Materials Chemistry and Physics 251 (2020) 123001

Contents lists available at ScienceDirect

Materials Chemistry and Physics

journal homepage: www.elsevier.com/locate/matchemphys

# Design and characterization of mechanically stable, nanoporous $TiO_2$ thin film antimicrobial coatings for food contact surfaces

Eduardo Torres Dominguez [a], Phong Nguyen [a,1], Annika Hylen [d], Matthew R. Maschmann [b], Azlin Mustapha [c], Heather K. Hunt [a,*]

[a] Department of Biomedical, Biological & Chemical Engineering, University of Missouri, 1404 Rollins St., 263 AEB, Columbia, MO, 65211, USA
[b] Mechanical & Aerospace Engineering, University of Missouri, E3413 Lafferre Hall, Columbia, MO, 65211, USA
[c] Food Science Program, University of Missouri, 1404 E. Rollins St., 246 Stringer Wing, Columbia, MO, 65211, USA
[d] Department of Biomedical Engineering, Saint Louis University, McDonnell Douglas Hall 3450 Lindell Blvd. St., Louis, MO, 65211, USA

## HIGHLIGHTS

- The coating's microstructure was the main cause of the variations observed in photocatalytic activity.
- The coating was macroscopically even and showed rhombohedral microstructure.
- Sintering temperature and aging time were significant synthetic factors.
- A combination of sintering temperature and aging time gives maximum photocatalytic activity.
- The hardness for the photocatalytically-optimized coating reported in this work was 2.6 GPa.

## GRAPHICAL ABSTRACT

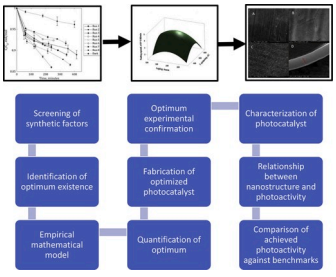


## ARTICLE INFO

*Keywords:*
Thin film
Sol-gel process
Mechanical properties
$TiO_2$
Photocatalytic
Porous material

## ABSTRACT

To improve food safety during food processing, we developed a titanium dioxide, photocatalytic coating that can be applied to standard stainless-steel food contact surfaces (FCS) via a sol-gel method. These thin, self-assembled, porous coatings have the potential to reduce surface cross-contamination in food processing environments when used in combination with oxygen, water, and ultraviolet (UV) light through photocatalytic processes. Under these conditions, the coating releases reactive oxidative species (ROS), the amount of which is directly related to the coating's photocatalytic activity; ROS are responsible for killing microorganisms. In this study, a quadratic mathematical model is used to optimize the relationships among synthetic parameters, including sol-gel aging time and sintering temperature, and the resulting photocatalytic activity of the coatings. Using statistical analysis, the coatings synthesized using 223 h aging time and 507 °C sintering temperatures were predicted to yield maximized photocatalytic activity within the experimental range. We verified this prediction experimentally, and compared the relationships between photocatalytic activity and the areal porosity of the photocatalytically-optimized coatings to determine how the porosity of the coatings impacted their photocatalytic activity. Lastly, in an effort to assess real-life applications, the mechanical stability of the photocatalytically-optimized coatings was evaluated using nanoindentation and pencil hardness testing. By tailoring the coatings' physicochemical

* Corresponding author.
*E-mail addresses:* etd2v@mail.missouri.edu (E. Torres Dominguez), Phong.nguyen@mail.missouri.edu (P. Nguyen), Annika.hylen@slu.edu (A. Hylen), maschmannM@missouri.edu (M.R. Maschmann), mustaphaA@missouri.edu (A. Mustapha), hunthk@missouri.edu (H.K. Hunt).
[1] Present address: Department of Chemical Engineering, University of California – Santa Barbara, Santa, Barbara, CA 93106-5080, USA.

https://doi.org/10.1016/j.matchemphys.2020.123001
Received 31 December 2019; Received in revised form 23 March 2020; Accepted 30 March 2020
Available online 19 April 2020

properties to optimize for photocatalytic performance and mechanical stability, we can create photocatalytic coatings for food contact surfaces that have the potential to prevent or minimize cross-contamination during food processing.

## 1. Introduction

Photocatalytic coatings have been touted as some of the most promising antimicrobial coatings (AMCs), due to their nontargeted disinfection action of different microorganisms [1]. They are typically formed from metal oxide materials, such as titanium dioxide ($TiO_2$), zinc oxide (ZnO), and tin oxide ($SnO_2$), which produce various reactive oxygen species ($^1O_2$, $O_2^{\bullet-}$, and $^{\bullet}OH$) when irradiated with ultraviolet (UV) light in the presence of water or moisture. Of these materials, $TiO_2$ is the flagship component of photocatalytic AMCs due to its ability to generate a high rate of ROS [2] and due to its ability to generate hydrogen peroxide ($H_2O_2$) from $^{\bullet}OH$ in the presence of water and UV light ($H_2O_2$ also has a known antimicrobial effect) [3–5]. Although published results are promising in terms of microbial inactivation [6], $TiO_2$-based AMCs have found little industrial applications because the durability (or mechanical robustness) of the coatings remains a standing issue that must be addressed before the coatings can be effectively translated to real-world applications [7].

As a broad concept, durability is related to the AMCs' ability to withstand damage. Damage of the integrity of the AMCs due to normal use (wear/scratching) can negatively affect the coatings' antimicrobial activity, or in extreme cases, cause the detachment of coatings from substrates and the termination of the antimicrobial activity altogether [8,9]. Moreover, if the coating delaminates from the surface, it can contaminate the food product. Depending on the specific application within the food production process, the coatings may be exposed to rinsing, brushing, ice pigging, hot water, steam, detergents, and hydrogen peroxide, among other stressors. The application of these stressors may deteriorate coatings by increasing surface roughness, scratching, cracking, and/or detachment from the substrate. To avoid this, the AMCs must be designed not only to demonstrate antimicrobial activity, but also to meet performance metrics regarding utility, such as various measures of durability, as governed by stringent regulatory standards applied worldwide [10–13].

The mechanical stability of antimicrobial coatings may be assessed through the measurement of various mechanical properties, including abrasion, adhesion, hardness, hydrophobicity, surface roughness, and antimicrobial agent migration [7]. Many of these properties are significantly influenced by the composition, microstructure, synthetic parameters, and the coating or deposition method used to produce the coatings [14–18]. These properties can be assessed by techniques such as nanoindentation, pencil hardness testing, tape testing, rotating abrader testing, and profilometry [19], respectively. When used in conjunction with standard materials characterization techniques, such as X-ray diffraction, spectroscopy, and electron microscopy, researchers can gain a holistic understanding of the nature of the coatings and how various synthetic parameters impact the resultant compositional, structural, and mechanical properties, in addition to the materials' antimicrobial activity.

In this work, we first explore how to design sol-gel based, $TiO_2$ coatings that *simultaneously* demonstrate optimized photocatalytic activity and adequate mechanical robustness (defined by hardness elastic modulus, and wear). In particular, we explore the impact of areal porosity (i.e., the coating's surface area) on the photocatalytic activity and mechanical resistance. Then, we present the design, synthesis, deposition, and evaluation of a photocatalytically-optimized nanostructured, porous, $TiO_2$ coating. Throughout this study, we use a standard method for the determination of photocatalytic activity as a way to compare our coatings with existing literature for similar coatings, when available. Lastly, we explore the mechanical properties of the resulting photocatalytically-optimized coatings in order to determine their durability.

## 2. Materials and methods

### 2.1. Design of experiment

The fundamental physics and chemistry underlying the formation of the bulk coating microstructure during sol-gel synthesis can be examined from two fronts: i) the size and extent of branching (gelation) of the sol species prior to coating deposition, and ii) evaporation of the solvents from the gel during coating deposition. For the former, hydrolysis and polymerization reactions play a large role in the branching process and are influenced by the following variables, potentially among others [20]: type and concentration of precursor, type of solvent, catalyst (acid or base), pH, presence of templating agent (which did not play any role in the degradation mechanism because it was removed during the coating's sintering step, but was responsible for the spatial structure of the pores in the coatings), time of reaction (aging time), and sintering temperature. For the latter, the following variables influence evaporation of the solvents during coating deposition [20]: temperature, relative humidity surrounding the coating, solvent's vapor pressure, size, and extent of branching of the gel, size of pores, coating thickness, relative rates of condensation reaction and evaporation, and pull-up speed (for the dip coating process) or spinning speed (for the spin coating process). Spin coating was chosen over dip coating because it has two relative advantages: (1) the radially outward flow driven by the centrifugal force allows for the creation of thinner coatings, and (2) the coating's thickness is more uniform due to the spin-off action, provided the viscosity of the sol-gel is not shear dependent [20]. Additionally, once the coating is deposited on the substrate, the microstructure can be further affected by the heating rate and the temperatures employed for the heating ramp of the sintering process (the process by which the particles of the coating spatially rearrange when temperature is increased) [20,21]. Control of these variables allows researchers to customize the coating's microstructure and its resulting properties.

However, attempting to control all of the variables at the same time is an arduous task with many likely confounding factors. Based on prior literature data on similar coatings [22–24], and particularly on the degree of accuracy that is possible to achieve for controlling the variables, we identified five synthetic factors that appear to significantly influence the coatings' microstructure (see Table 1: type of synthetic protocol, templating agent to precursor ration, aging time, spinning speed, and sintering temperature) and affect one or more of the fundamental variables listed above.

In this study, we used a full, two-factorial design of experiments, shown in Table 2, to evaluate the impact of (1) the type of protocol, (2) the templating agent to precursor ratio, (3) the aging time, (4) the spinning speed, and (5) the sintering temperature, on the photocatalytic activity of the resulting coating. In this type of design of experiment, each synthetic factor is varied at two extreme levels. The number of runs and the specific combinations of synthetic factors for each run were chosen following the procedure proposed by Lazic [32]. The eight runs were triplicated. The photocatalytic activity, expressed as fading speed (the rate at which a synthetic dye, methylene blue, was faded), was assessed for each coating following the test described in section 2.3.3, and was used as the response of the experiments. This method of photocatalytic activity assessment (ISO 10678:2010) was selected because, although multiple tests can be found to demonstrate an AMC's photocatalytic activity and its consequent antimicrobial activity, the

**Table 1**
The variables impacting the size and extent of branching and evaporation of solvent rate of the coatings were changed experimentally by means of five different synthetic factors: type of synthetic protocol, templating agent to precursor ratio, aging time, spinning speed, and sintering temperature. Observe that some factors may influence more than one variable.

| Synthetic factor | Affected variable |
|---|---|
| Protocol 1/Protocol 2 | Catalyst, solvent, type of precursor [25,26]. |
| Templating agent to precursor ratio (Ti:EO)[1] | Size and shape of pores [27]. |
| Aging time | Size and shape of pores, extend of polymerization reaction, gel viscosity [28,29]. |
| Spinning speed | Coating thickness, drying rate, extend of polymerization reaction [20,30]. |
| Sintering temperature | Pore size, coating densification [31]. |

[1] Pluronic P123, poly(ethylene oxide)-poly(propylene oxide)-poly(ethylene oxide), was chosen as the templating agent because its molecular chain length produces micelles in the range of 20–100 nm diameter in the presence of ethoxides, water, and ethanol.

application of standard tests, such as ISO 10678:2010, is the most convenient way to assess this parameter because it allows for comparison of photocatalytic activity between AMCs [1].

In the standard photocatalytic activity test (ISO 10678:2010), the ROS generated by the coating(s) are assessed by means of the rate of degradation, via oxidation, of the methylene blue dye, which is measured spectrophotometrically. The photocatalytic activity is better interpreted as the rate at which $H_2O_2$ (a derivative of $O_2^{\bullet-}$), $^{\bullet}OH$, and $^1O_2$ (collectively, the ROS) are generated [1]. ROS generation by semiconductor materials (which include $TiO_2$) can be linearly related to their antibacterial activity by means of Equation (1) obtained from experimental data using *Escherichia coli* as target cells [2]:

$$Y = -0.00138X \quad (1)$$

where $Y$ is the survival rate ($\log(N_t/N_0)$, $X$ is the average concentration of total ROS in micromolar units, $N_t$ is the number of viable colonies in contact with the semiconductor nanoparticles for 2 h with no UV light irradiation, and $N_0$ is the number of viable colonies after 2 h of UV irradiation in the presence of different semiconductor nanoparticles. The negative sign of the $X$ factor in Equation (1) means that the higher the ROS concentration, the lower the survival rate of the cells. Equation (1) was determined on the presumption that the antimicrobial effect of semiconductor materials is due to oxidative stress, which may be bacteria-specific, but for initial or screening studies, this provides a starting point for comparing coatings.

However, for photocatalytic coatings to be industrially viable as antimicrobial coatings, they must perform with and withstand deterioration from the cleaning methods they will be used in conjunction with. Given this, a starting point coating should demonstrate, firstly, a level of antimicrobial activity. Because the durability of the coating is determined by the minimum specifications needed in specific processes, we first focused on optimization of the coating's photocatalytic activity, followed by attending to the relationship with the coating's mechanical properties after we had determined the optimal synthetic parameters to produce a photocatalytically-optimized coating.

### 2.2. Coating fabrication

Coatings were prepared by sol-gel processing using titanium (IV) ethoxide as a precursor following two different protocols [25,26], see Table 2. For Protocol 1, the acid-precursor mixture was formed by mixing 0.80 g of fuming hydrochloric acid (which served as the catalyst for the hydrolysis and the condensation reactions) (37%, Honeywell Fluka, USA, the catalyst) with 1.0 g of titanium ethoxide (20% titanium in ethanol, Sigma-Aldrich, USA) while stirring at 800 rpm. In a separate vial, 0.25 g or 0.11 g (depending on the titanium to ethylene oxide Ti:EO ratio) of surfactant, Pluronic P123 (~5800 molecular weight, Sigma-Aldrich, USA) that was dissolved in 4.25 g of ethanol (≥99.5%, Decon Laboratories, USA), was used as the templating agent and was then added to the acid-precursor mix. The complete mixture was stirred at 25 °C using a magnetic bar spinning at 800 rpm by means of a hot plate (RCT basic and ETS-D5, IKA, Germany). The resultant pH was ~0. For more details see Atefyekta's publication [25].

For Protocol 2, 6.4 g of deionized water and 1.0 g of titanium ethoxide were mixed for 5 min under stirring at 1200 rpm. The resulting powder was filtered and washed five times with deionized water and then reacted with a mixture of 5.3 g of hydrogen peroxide solution (30% wt/wt in water, Sigma-Aldrich, USA) and 15 g of deionized water at 0°C in a water-ice bath. The mixture was cooled for four days at 4 °C with no further mixing until the polymerization was complete. Afterward, the gel was combined with a solution of P123 and 4.25 g of ethanol (≥99.5%, Decon Laboratories, USA) similar to that used for the first protocol: 1.00 g of titanium ethoxide/0.25 g of P123 or 1.00 g of titanium ethoxide/0.11 g of P123 were used to obtain 0.5 or 1.2 titanium to ethylene oxide molar ratios (Ti:EO), respectively. See Urade for details of the Ti:EO calculation [27]. The as-prepared sol-gels and the templating agent were mixed to allow the formation of two different surfactant phases [27]. Then, the resulting gels were aged inside of closed vials at room temperature for either 1 h or 240 h after the mixture was completed. For both protocols, the sol-gels were deposited on clean, food-grade standard stainless steel typically used in food industry, square substrates with dimensions 1.8 cm × 1.8 cm (Stainless-steel AISI 304, finishing No. 2B, 0.203 mm thick, Ulbrich, USA) using a spin coater (WS-400BZ-6NPP/Lite, Laurell, USA). The spin coat cycle consisted of two steps: (1) 15 s at 200 rpm for dispensing the gel on the substrate and (2) 45 s at top velocity (to obtain different coating thicknesses [20]) to

**Table 2**
Design of experiment to screen synthetic factors influencing the photocatalytic activity of the coatings. Protocol refers to protocol 1 or 2; titanium to ethylene oxide molar ratio (Ti:EO); aging period of time (t aging); spinning velocity, revolutions per minute (rpm), thermal sintering temperature (T sintering), fading speed ($r$), and photocatalytic efficiency (ε).

| Run | Synthetic factors | | | | | Response | | Coating's properties | | |
|---|---|---|---|---|---|---|---|---|---|---|
| | Protocol | Ti:EO[1] | $t_{aging}$, h | rpm | $T_{sintering}$, °C | $r$, x$10^{-9}$ M/min | $\varepsilon$, x$10^{-3}$% | Areal porosity | Thickness, nm | Pencil hardness |
| 1 | 1 | 1.2 | 1 | 6000 | 400 | 3.5 ± 0.10 | 4.8 ± 0.3 | 42 | 608 ± 45 | –[2] |
| 2 | 1 | 1.2 | 1 | 2000 | 600 | 2.2 ± 0.18 | 2.7 ± 0.5 | 24 | 649 ± 54 | –[2] |
| 3 | 1 | 0.5 | 240 | 6000 | 400 | 4.0 ± 0.06 | 5.6 ± 0.1 | 38 | 1056 ± 96 | 6B |
| 4 | 1 | 0.5 | 240 | 2000 | 600 | 2.7 ± 0.08 | 2.8 ± 0.2 | 34 | 1200 ± 77 | 5B |
| 5 | 2 | 1.2 | 240 | 6000 | 600 | 3.3 ± 0.08 | 4.0 ± 0.2 | ~0 | 1436 ± 215 | 4B |
| 6 | 2 | 1.2 | 240 | 2000 | 400 | 4.9 ± 0.14 | 7.6 ± 0.3 | 95 | 1909 ± 135 | HB |
| 7 | 2 | 0.5 | 1 | 6000 | 600 | 2.4 ± 0.09 | 3.5 ± 0.3 | ~0 | 724 ± 38 | 2B |
| 8 | 2 | 0.5 | 1 | 2000 | 400 | 4.2 ± 0.23 | 7.0 ± 0.6 | 84 | 821 ± 50 | 1B |

[1] The ratio of the number of titanium atoms in solution to the number of ethylene oxide groups in solution was chosen because the surfactant/water/ethanol phase diagrams are built based on this relationship [33–35].
[2] The coatings were so cracked that it was impossible to measure the pencil hardness reliably.

either 2000 or 6000 rpm. The relative humidity inside the spin-coater chamber was maintained at 60% using a flow of humid air coming from a custom-built humidifier. Once on the substrate, the deposited coatings were dried inside a custom chamber set at 90% relative humidity. Finally, the samples were thermally sintered for 4 h at two different temperatures in a muffle furnace (Lindberg Blue M, Thermo Scientific, USA): 400 or 600 °C, which are known to be the minimum temperature values to obtain anatase and rutile phases, respectively [21]. All the aforementioned coating fabrication conditions are summarized in Table 2.

### 2.3. Characterization

#### 2.3.1. Structural and quality analysis

The structures of the AMCs were elucidated using X-ray diffraction (XRD) (Ultima IV, Rigaku, Japan) using a Cu K-α source, 0.1518 nm wavelength, 40 kV, 5–80° two theta, stepsize-0.02, at 2°/min using $TiO_2$ powder obtained under exactly the same conditions as those used to fabricate the optimized coating. The powder was obtained from the gel that was used to spin coat the substrates. The gel was dried and sintered using the same heating ramp employed to sinter the optimized coatings. Powder instead of the actual coating was used because of the coating's thin thickness and the substrate's high roughness produced erratic results during the X-ray diffraction measurements.

Topographical information about the coatings, namely surface continuity, coating quality, pore size, pore direction, and coating thickness were obtained by Scanning Electron Microscopy (SEM). The microscope (FEI Quanta 600, ThermoFisher Scientific, USA) was operated at 30 keV potential, smallest aperture, and spot size 3 nm. Since $TiO_2$ is a semiconducting material, no additional coating for SEM was needed.

The complete removal of Pluronic P123 from the coating was verified via Energy Dispersive Spectroscopy (EDS) (Quanta 200 with Xflash6, Bruker, USA). The areal porosity of the coatings was estimated via areal image analysis of the SEM micrographs. The micrographs of the top of the coatings were analyzed using ImageJ software (Public domain, National Institute of Health, USA) with −144 brightness and 0.117 threshold values. Each micrograph was imaged with the same horizontal field width (HFW 1.71 μm) to maintain consistency in the data analysis. We assumed that on the surface level, the areal porosity observed corresponds to cylindrically-shaped, vertical pores, and that the total area of the top circular daces of those cylinders is directly proportional to the total volume of pores ($V_{voids}$) along the lateral surface ($V_{coating}$). Equation (2) was used to estimate the areal porosity:

$$P = \frac{\sum V_{voids}}{V_{coating's\ total}} * 100\% = \frac{\sum Area_{dark}}{Area_{total}} * 100\% \quad (2)$$

where $Area_{dark}$ corresponds to the area of each pore observed on the SEM image and $Area_{total}$ corresponds to the total area of the top view image analyzed (more details are provided in the Supplementary Information file).

The roughness of the coatings' surfaces was evaluated using two methods: (1) atomic force microscopy(Innova, Bruker, USA) using a silicon probe (ACTA 50, AppNano, USA) in tapping mode, 2.0 μm of scan range, at 1.0 Hz scan speed, and (2) optical profilometry (Wyko NT 9100, Veeco Instruments, USA) using high definition vertical scanning interferometry for samples that exhibited high roughness. After coating the substrate, the hydrophobicity of the coatings was evaluated using a standard goniometer (200-F4, Ramé-Hart, USA).

#### 2.3.2. Mechanical analysis

Elastic modulus and hardness of the optimized coatings were tested by nanoindentation (G200, Agilent, USA) with a Berkovich diamond tip (Micro Star Technologies, USA). Each test consisted of a series of 10 loading and unloading steps and a maximum load of 200 mN. The modulus and hardness were evaluated at each unloading step using the standard Oliver-Pharr method [36]. Each coating surface was sampled in 25 locations. The tip did not experience torque in a uniaxial test.

Wear was assessed with the same nanoindenter using a sapphire spherical tip (200 μm diameter, Micro Star Technologies, USA). Each wear test consisted of 100 unidirectional scratches along a 100 μm long wear path. Wear was conducted under a constant normal load of 50 mN and a speed of 50 μm/s.

Bulk hardness was assessed by means of the pencil hardness test. The test consists of making straight lines on the coating using pencils of decreasing hardness. This operation is performed using a special pencil holder of mass 500 g. The holder grasps a pencil at a 45° angle to the surface of the substrate and is dragged across the substrate against the grain of the film. The coating is examined under a 40 × magnification to determine whether the film has been scratched. The result of the test comes when a pencil lead that is not able to scratch the coating is found. The hardness is then expressed in terms of a scale that ranges from 6B (the softest), 5B, 4B, *etc.* to 6H (the hardest), 5H, *etc*. The scale has intermediate values designated as HB and F, which gives a total of 14 hardness values. This method is based on the standard ASTM D 3363-05 [37].

#### 2.3.3. Photocatalytic activity

The photocatalytic activity of the coatings was tested following the international standard ISO 10678:2010 [38]. In this test, the samples were preconditioned by placing them in the dark in 11.3 mL of 2.0x10-5 M methylene blue (this dye is specified by the standard) (84%, Fisher Scientific, USA) (aq) solution resting for 12 h or until the dye concentration ceased to change. After the preconditioning step, the samples were rinsed with deionized water, placed in 11.3 mL of $1 \times 10^{-5}$ M aqueous solution of methylene blue and then irradiated with a 6 Watt UV-A lamp (365 nm, 6 Watts, UVP UVL-56, Analytikjena, USA). The aqueous solution was stirred every 20 min. Fig. 1 is a schematic representation of the test setup. The ROS generated by the photocatalyzed reaction faded the methylene blue as time passed. The decreasing methylene blue absorbance was measured using a UV–Visible light spectrophotometer (Varian Cary 50 Bio, Agilent, USA) operated in absorbance mode. Absorbance values were recorded at 665 nm. In order to correlate the absorbance to the concentration of the dye, a calibration

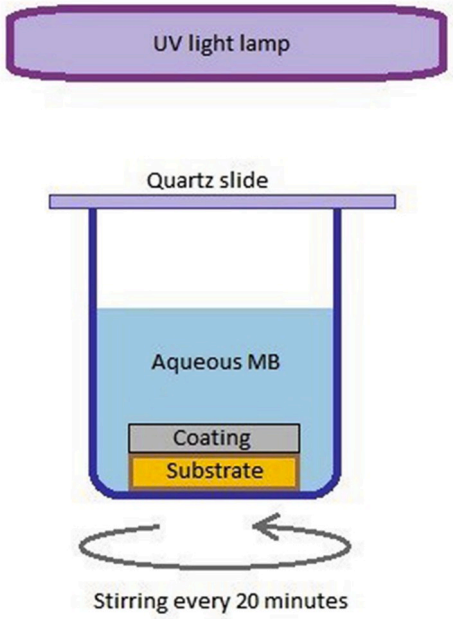


**Fig. 1.** Schematic of the main elements to test photocatalytic activity. The samples are removed from inside the beaker and returned to it after measuring the absorbance with a spectrophotometer (not shown) in absorbance mode.

curve was created. The ISO standard specifies a 10 $cm^2$ coating sample placed in 35 mL of dye. Since our coating samples had an area of 3.24 $cm^2$, we used a proportional volume of dye solution, namely 11.3 mL. Similar experiments were run but with no UV light irradiation (dark), which served as controls of the test. For more details on the photocatalytic activity test refer to the standard [39]. The reported value expressed as fading speed was calculated using Equation (3):

$$fading\ speed\ [M/min] = C_t \frac{1}{t} ln \frac{C_0}{C_t} \quad (3)$$

where $C_t$ is the concentration (molar) of methylene blue (determined by UV visible spectrophotometry and the application of Beer-Lambert Law) at time $t = 180$ min, and $C_0$ is the initial concentration ($1.00x10^{-5}\pm0.1$ M) of methylene blue (aq) at the beginning of the fading experiment. Additionally, the photocatalytic efficiency was calculated using the equation established in the international standard for this purpose:

$$\varepsilon = Photocatalytic\ efficiency,\ \% = \frac{Specific\ photoactivity,\ mol/(m^2 h)}{Average\ photon\ UV\ radiation\ intensity,\ mol/(m^2 h)} 100\% \quad (4)$$

### 2.4. Optimized coating fabrication

The optimized coating fabrication procedures were exactly the same as those described in the coating fabrication for screening of synthetic factors. However, only Protocol 2 was used and the following synthetic factors were fixed: 1.2 titanium to ethylene oxide ratio, and 4000 rpm spinning velocity (see Table 3). The experiment shown in Table 3 was used to collect enough elements to form a second-order polynomial equation. The center point was located by setting the aging time and sintering temperature at their midpoints regarding the lower (140 h and 360 °C) and upper level values (340 h and 640 °C). This design used five center points to check the variability (standard deviation) of the entire experiment, as well as the significance of the mathematical coefficients and the lack of fit of the obtained mathematical model [32]. Like in the screening of synthetic factors, the fading speed was assessed and assigned as the experiment response (See Table 3).

An additional batch of optimized coatings was prepared exactly in the same way as described above but using a much more polished substrate (see section 3.4 for a discussion of the reasons for doing so). Clean, 1.8 cm × 1.8 cm square substrates (Stainless-steel AISI 304, finishing No. 8 mirror-like, 0.203 mm thick, Ulbrich, USA) were spin-coated to obtain coatings whose surface was less affected by the substrate's topography, and therefore, made them more useful for nanoindentation testing purposes [40].

**Table 3**
Central composite or second-order rotatable design of experiment. In this full design the relevant experimental points are: central (or null) 500 °C and 240 h; star-like 340 °C, 640 °C, 340 h and 140 h; core 600 °C, 400 °C, 312 h, and 158 h. The coded α value for the star-like points is 1.414; $t_{aging}$ is aging time; $T_{sintering}$ is sintering temperature; $r$ is fading speed; and $\varepsilon$ is photocatalytic efficiency.

| Trial | Synthetic factors | | Response | |
|---|---|---|---|---|
| | $t_{aging}$, hours | $T_{sintering}$, °C | $r\pm0.109$, x $10^{-9}$ M/min | $\varepsilon\pm0.2$, x$10^{-3}$% |
| 1 | 312 | 600 | 2.96 | 3.2 |
| 2 | 158 | 600 | 3.30 | 3.8 |
| 3 | 312 | 400 | 2.96 | 3.2 |
| 4 | 158 | 400 | 2.98 | 3.2 |
| 5 | 140 | 500 | 3.82 | 4.7 |
| 6 | 340 | 500 | 2.96 | 3.2 |
| 7 | 240 | 360 | 2.60 | 2.7 |
| 8 | 240 | 640 | 2.86 | 3.1 |
| 9 | 240 | 500 | 4.42 | 5.8 |
| 10 | 240 | 500 | 4.43 | 5.8 |
| 11 | 240 | 500 | 4.18 | 5.4 |
| 12 | 240 | 500 | 4.37 | 5.7 |
| 13 | 240 | 500 | 4.39 | 6.5 |

## 3. Results and discussion

### 3.1. Screening of synthetic factors experiment

In the present work, the triplicated values of the fading speeds determined for each run were averaged and used as the run's response (see Table 2). The results of the design of experiments were analyzed using a statistical computer program (Minitab 18, Minitab, USA) which showed that aging time and sintering temperature were the only synthetic factors that affect the fading speed, with a statistical significance within a 95% confidence interval. Pareto and normal plots of the effects were constructed to confirm the significance of the factors (Figs. S1 and S2 of the Supplementary Information document). The statistical analysis also showed that while there is an interaction effect between spinning speed and templating agent/precursor ratio, the interaction is not statistically significant. It is important to highlight that the initial screening of synthetic factors provided *a priori* insight about the location of the optimum values of the synthetic factors. Run 6 of Fig. 2 certainly can be considered as a combination of variables that gave the highest fading speed among all the other combinations of synthetic factors. Therefore, Run 6 was chosen as a reference to locate the center point for the experimental determination of the mathematical model. Fig. 2 is a graphical summary of the decreasing, normalized concentration of methylene blue as a function of time. The steeper the curve, the higher the photocatalytic activity.

The microstructure of the coatings obtained by different combinations of synthetic factors was the predominant feature responsible for the variations observed in photocatalytic activity. Fig. 3 illustrates three exemplars that covered the range of macro/microstructures obtained from the set of eight experiments of Table 2 after the sintering step. The SEM images of the eight runs may be found in the supporting information document. The microstructure of the coatings was affected by three factors: the addition of a surfactant agent, the ratio between the surfactant agent and the titanium ethoxide, and the aging time. For example, when a triblock copolymer surfactant, such as P123, was placed in a selective solvent, such as ethanol, it would form at least four different micelle types or phases after undergoing an evaporation-induced self-assembly process [34], see Fig. 4. The four phases are: 1) rhombohedral with cubic lattice pattern; 2) 2D hexagonal with

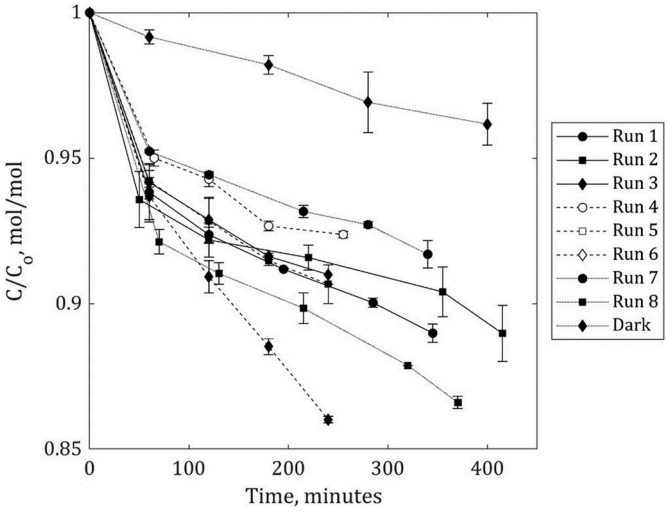


**Fig. 2.** Overall fading test comparison. The coatings obtained from the eight combination of fabrication parameters were tested for photocatalytic activity at regular periods. Certain combinations, such as Run 6 and Run 8 showed the highest photocatalytic activity, while Run 7 and Run 4 the lowest. Error bars are on all points, but bars are smaller than the symbol used.

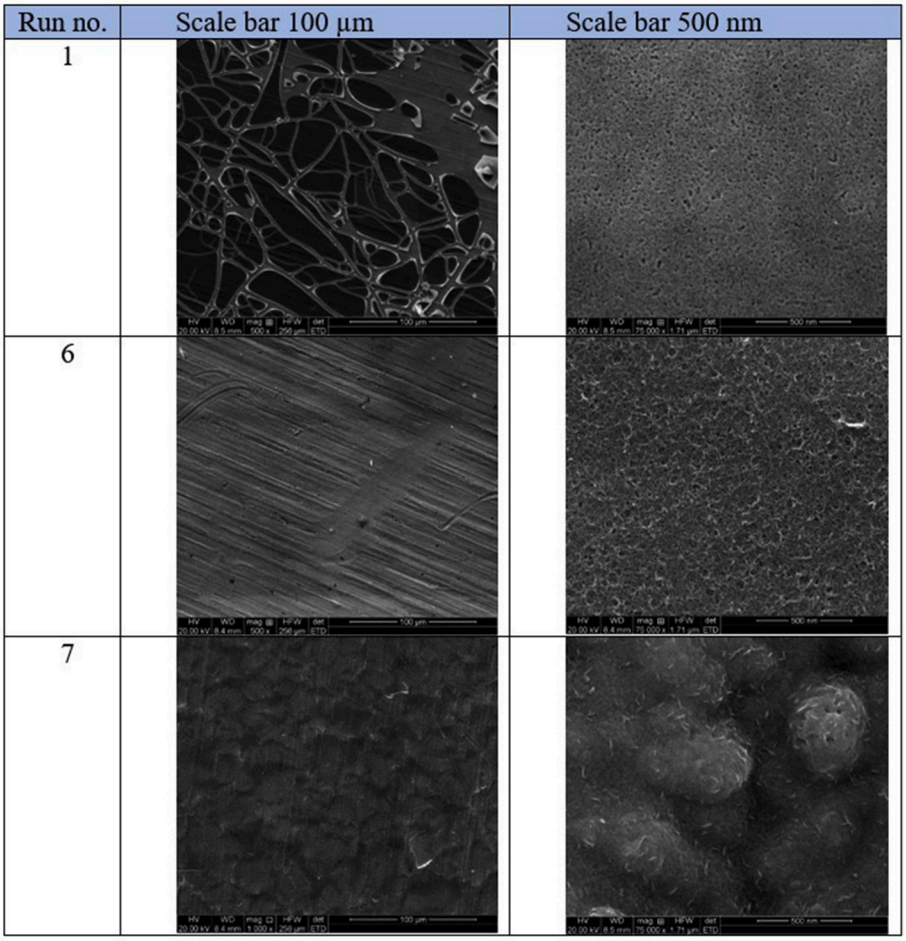


**Fig. 3.** Macrostructure and microstructure by SEM of $TiO_2$ coatings from three different runs. The macro and microstructures of the coatings are influenced by all the synthetic factors but especially by the sintering temperature. Run 1 yielded a completely cracked coating with gyroid microstructure. Coating from Run 6 was macroscopically even and showed a rhombohedral microstructure. The coating from Run 7 was even but showed some delamination and completely sintered microstructure.

cylindrical micelles arranged in a 2D hexagonal lattice; 3) gyroid also known as double-gyroid topology; and d) lamellar with planner micelles. The various Ti/surfactant ratios, when combined with the aging times, yielded two different surfactant phases exhibiting nanostructured, open pores [27]: gyroid and rhombohedral, that correspond to microstructures obtained from run 1 and run 6, respectively. These phases resulted from the interplay of solution composition and ambient relative humidity in addition to metal-surfactant ratio and aging time [28]. Micelle phases were formed in the liquid state of the sol-gel process. However, the micelles' spatial configurations were retained due to the stiffness that polymerization (e.g. aging) gave to the gelled structure after the methanol and water from the gel had evaporated [20]. During the sintering step, the surfactant used to form the micelles in the gel was combusted, leaving a porous structure behind if the temperature is 400 °C, like in run 1 and run 6, or a completely sintered granular surface when the temperature is 600 °C, such as in run 7.

It can be observed in Fig. 5 that areal porosity was linearly correlated to fading speed. The highest values of fading speed corresponded to the highest values of areal porosity, which belonged to Run 6 and Run 8. The opposite was true for coatings with no pore microstructure, for which some of the lowest fading speeds were recorded, namely Run 5 and Run 7. Although important, porosity was not indispensable for achieving photocatalytic activity, as has been observed in nonporous photocatalytic coatings [41], just not as much as porous coatings. Returning to areal porosity, values larger than 80% double the photocatalytic activity of the coatings compared to nonporous coatings, as can be observed in Fig. 5. It can also be observed on the plot that all the coatings obtained from Protocol 1 were located around 40% porosity and $3.00 \times 10^{-9}$ M/min fading speed, while coatings from Protocol 2 were positioned in two separate groups: (a) around 85% porosity and $5.00 \times 10^{-9}$ M/min and (b) around 0% porosity and $3.00 \times 10^{-9}$ M/min. Protocol 1 can be further subdivided into two groups based on the run's position on the plot of Fig. 5: Run 2-Run 4 and Run 1-Run 3 corresponding to 600 °C or 400 °C sintering temperature, respectively. A careful examination of the fabrication parameters corresponding to each run, Table 2, and Table S1 (supplementary information) showed that the *microstructure of the coatings at nanoscale levels varied alternatively from porous to nonporous depending on the low or high set value (400 °C or 600 °C) of the sintering temperature*. This fact led us to conclude that the sintering temperature was the most influential parameter that definitely affected the areal porosity present in the coatings. The high and low values of sintering temperature separated the coatings of Protocol 1 and Protocol 2 into pair groups on the plot shown in Fig. 5, providing additional evidence of the sintering temperature's influence on the areal porosity of $TiO_2$ coatings, which in turn affected the photocatalytic activity. The importance of the sintering temperature as a fabrication parameter was later confirmed through optimization experiments (See mathematical model section 3.2).

Sintering is a complex process in which four competing subprocesses occur: interfacial area reduction (elimination of porosity), self-assembly agent calcination (porosity generation), grain growth, and phase transformation. The progress of each sub-process relative to the others depends on the period of time that has elapsed, the volume fraction of crystals (or its absence in case of amorphous materials), and the sintering temperature. In the specific case of $TiO_2$, the effect of sintering temperature in the resulting coatings when a tri-block copolymer was used as surfactant is as follows [42]: surface area (determined by the Brunauer-Emmett-Teller (BET) method) reduction from 214 to

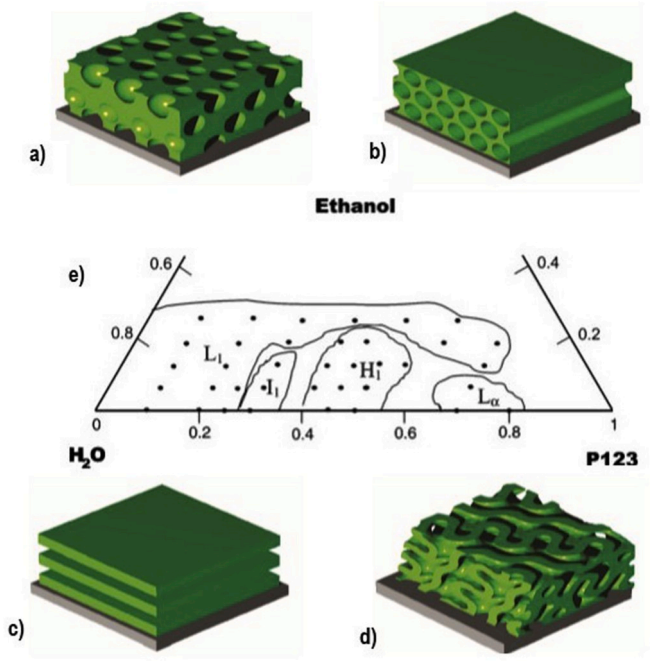


**Fig. 4.** P123 forms four different well-ordered nanostructured micelle patterns in presence of water and ethanol. The renderings were created using the software NANOCELL for the triblock copolymer P43 for silica thin films: a) rhombohedral, b) 2D-hexagonal, c) lamellar, and d) gyroid [27]. The ternary phase diagram e) shows the concentration regions where P123 forms the gyroid ($L_1$), rhombohedral ($I_1$), 2D-hexagonal ($H_1$), and lamellar ($L_\alpha$) phases [34].

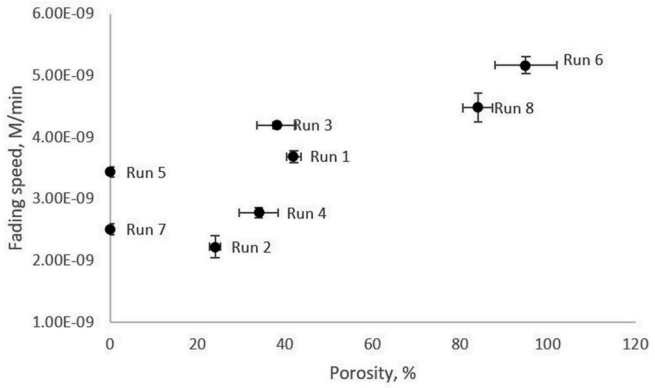


**Fig. 5.** Fading speed is positively correlated to nanoscale porosity, which in turn, is influenced by the sintering temperature, as can be seen from the location of the fading speed-porosity points grouping in pairs corresponding to the high and low temperatures levels used in the screening of synthetic factors experiment.

119 $m^2/g$ and crystallite size growth from 9.8 to 20.5 nm when the sintering temperature was increased from 400 to 600 °C.

In addition to their main function of serving as screening of synthetic factors technique, the eight runs also showed both favorable and unfavorable conditions for the formation of macroscopically continuous coatings. A deeper investigation of the reasons for the observed macroscopic cracks in coatings from Run 1, Run 2, and Run 3, and the absence of them on the rest of the runs (see Table S1 in supplementary information) is out of the scope of the present work; however, it is possible that the aging time used caused a stiffening of the microstructure generated by the templating agent in the gel to a much higher degree for the gel from Protocol 1 than it did for the gel of Protocol 2. Although obtained from the same precursor (titanium ethoxide), it can be inferred that Protocol 1 yielded a branched mass fractal gel, while Protocol 2 produced a uniform (nonfractal) gel of aggregated particles [20]. It appeared that (1) the branched structure favored the development of stress at the interior of the coating during the deposition and drying steps, which resulted in crack formation, and that (2) the only parameter that can be varied of the five that were investigated here to avoid crack formation in coatings prepared from Protocol 1 was aging time. Particulates forming the gel of Protocol 2 could favor a low-pressure gradient between the pores of the drying coating and the ambient surroundings, decreasing the drying stress, which in turn, prevented crack formation.

Going further into an exploration of the cracked coatings, Run 1 and Run 2 had such cracked structures that their pencil hardness could not be determined, showing the influence of the catastrophic failures on the pencil hardness assessment and the limitations of the technique. The pencil hardness test is based on the identification of the pencil's tip, which did not produce damage on the coating to be assessed, which is supposed to be continuous and uniform. Since these characteristics were not met by the coatings obtained for Run 1 and 2, their values could not be stablished. In the same way, it seems that the type of protocol influenced the hardness of the rest of the coatings: coatings obtained from Protocol 1 tended to be softer than those produced by Protocol 2. This could be attributed to the agglomeration and more compact nature of the coatings obtained from Protocol 2, while those given by Protocol 1 were branched and spongy.

### 3.2. *Optimization of photocatalytic activity and mathematical model*

After determining that sintering temperature and aging time were statistically significant synthetic factors, we decided to evaluate what combination of sintering temperature and aging time yielded the best response for photocatalytic activity, as shown in Table 3. As a first attempt at this, we created and carried out a design of experiment that could generate a linear mathematical model of the relationships among aging time/sintering temperature and photocatalytic activity by creating coatings while varying sintering temperature and aging time and keeping the other factors (fabrication protocol, templating agent to precursor ratio, and spinning speed) constant. However, the experiments demonstrated (see Table S2 in Supplementary Information) that a linear mathematical model lacked fit, and therefore, was insufficient for an accurate mathematical description of the observations.

Therefore, we designed and performed a second-order rotatable design of experiments, varying the aging time and sintering temperature only. In this experiment, the synthetic factors were varied in four different levels that scanned the process conditions around the experimental center, namely 240 h aging time and 500 °C. The results of the design of experiment were statistically analyzed using Minitab's response surface analysis tool. The mathematical model obtained in the form of a regression equation (Equation (5)) along with its statistical descriptors are shown in Table 4. Using a confidence level of 0.05 ($\alpha = 0.05$) the linear term of sintering temperature and the aging time-sintering temperature interaction term were not significant and, therefore, could be removed from the mathematical model. In the same way, lack of fit was not significant and the $R^2$ value was close to 100, so the mathematical model was considered adequate.

A graphical representation of the coating's photocatalytic activity expressed as fading speed is shown in Fig. 6. It can be observed that a certain combination of sintering temperature and aging time gives an optimum (maximum) fading speed. The optimal values were 223 h of aging time and 507 °C of sintering temperature with an expected fading speed of $4.6 \times 10^{-9}$ M/min. Regarding the model, it can be said that the sintering temperature had the largest influence on the observed fading speed, followed by the aging time. These results are relevant since it has been found that (1) calcination temperature of sol-gel $TiO_2$ coatings deposited on titanium showed increased values of hardness, elastic modulus, and wear resistance [21]; and (2) unaged $TiO_2$–$SiO_2$ coatings

**Table 4**
The second-order rotatable design of experiment yielded a quadratic mathematical model whose main parameters are summarized below. The P-values were used to identify the mathematical model's significant coefficients. The mathematical model was also used to calculate the optimal aging time and sintering temperature. The graph shows the surface response within the experimental space.

| Coded coefficients (dimensionless) | | |
|---|---|---|
| Term | Coefficient | P-value |
| Constant | 4.548 | 0.000 |
| A, aging time | −0.329 | 0.001 |
| B, sintering temperature | 0.121 | 0.102 |
| AA | −1.021 | 0.000 |
| BB | −1.701 | 0.000 |
| AB | −0.151 | 0.241 |
| Fit | | |
| $R^2$ | 97% | – |
| Lack of fit | – | 0.242 |
| Optimization results | | |
| $t_{aging}$, hours | 223 | |
| $T_{sintering}$, °C | 507 | |
| Maximum fading speed, M/min | $4.39x10^{-9}$ | |

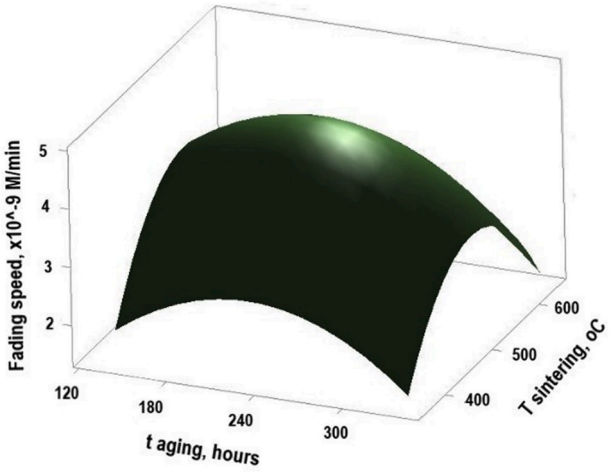


**Fig. 6.** The shape and position of the optimum conditions to reach the maximum fading speed can be better visualized by means of this surface plot of fading speed as a function of aging time ($t_{aging}$) and sintering temperature ($T_{sintering}$).

on titanium showed the best wear resistance while the wear rate increased with aging times varying from 1 to 10 weeks [29]. The authors of these two investigations agree that the improvements in the mechanical properties are due to the phase structure and grain size, namely, higher temperature produces more rutile phase (which is denser than anatase phase) and lower period of times produce smaller grains sizes. The same trend was observed in our research (see characterization of photocatalytically-optimized coating), however, the effects of temperature and aging time towards the optimum photocatalytic activity followed the opposite directions of those required for increased mechanical robustness.

$$Fading\ speed = 4.548 - 0.329(t_{aging}) - 1.021(t_{aging})^2 - 1.701(T_{sintering})^2 \quad (5)$$

### 3.3. Structural and quality analysis

#### 3.3.1. X-ray diffraction (XRD)

XRD analysis of the $TiO_2$ powder obtained using the same synthetic parameters that were used to produce the photocatalytically-optimized coating showed the anatase crystal phase only, see Table 5 and Fig. S3 in Supplementary Information. Relevant peaks from the XRD pattern were located at the following 2θ angles: 25.17, 38.23, 47.90, 55.01, and 62.60. The 2θ peaks at 25° and 48° confirm the anatase $TiO_2$ phase [43]. The crystallite size was calculated using Scherrer's equation:

$$\tau = \frac{K\lambda}{\beta cos\theta} \quad (6)$$

Where τ is the mean size of the crystalline domain, K is the shape factor (~0.9), λ is the X-ray wavelength (0.1518 nm), β is the line broadening at the maximum intensity (~0.0095 radians), and θ is the Bragg angle. The average crystallite size was calculated to be 15 nm. This value was set in context of the hardness and wear discussed in section 3.4.

#### 3.3.2. Contact angle measurement

Two contact angle measurements were performed on the photocatalytic-optimized coating using 2 μL of pure water as the testing liquid: with and without UV light illuminating the surface of the coating. Both tests showed that the coating was hydrophobic, but at different degrees. The coating's average contact angle for dark conditions (no UV light) was 61° while the coating's average contact angle after 30 min of UV light irradiation was 78°, meaning that the $TiO_2$ coating was more hydrophobic when irradiated with UV light. This difference showed the reason why $TiO_2$ has been extensively researched as the material of construction of coatings with potential self-cleaning applications [1]. Although the exploration of this behavior is outside the scope of this manuscript, it is possible that the generation of ROS by the $TiO_2$ in the presence of water and UV light, which also grants the coatings their antimicrobial activity, is also responsible of the change in hydrophobicity of the surface [44].

#### 3.3.3. Scanning electron microscopy

The complete removal of surfactant, solvents (water and ethanol), and catalyst (hydrochloric acid) after the sintering step was verified by Energy-Dispersive X-ray Spectroscopy (see Fig. 7). Titanium and oxygen were detected at low energies, close to the coating's surface, while the intensities of the peaks for iron, chromium, nickel, and manganese (the stainless steel main components) increased at medium-level energies, targeting the stainless steel substrate.

The micrographs of the photocatalytically-optimized coating showed it as a continuous and porous coating. No macroscopic or microscopic cracks were observed (see Fig. 8). The coating's thickness varied radially across the substrate, mainly because the gel was dispensed using a manual dispensing system rather than an automated one. The thicker zones were located around the center, while the thinner portions were found in the intermediate region between the center and the perimeter of the substrate. This thickness behavior is typical for spin-coated materials when an automatic gel dosing system is not employed [26]. The thickness of the coating in the intermediate region was around 690 nm. It is important to note that the periodic rippling observed in the micrograph A) of Fig. 8 are due to the substrate's surface, namely 2B

**Table 5**
Properties of the photocatalytic-optimized coatings on stainless steel 2B finishing.

| Property | Value |
|---|---|
| Crystal structure | Mainly anatase |
| Nanostructure orientation | Rhombohedral [27] |
| Pencil hardness | 2B |
| Photocatalytic activity, M/min | $4.31 \pm 0.6931x10^{-9}$ |
| Photocatalytic efficiency ε, % | $6.4 \pm 1x10^{-3}$ |
| Areal porosity | 50 ± 3% |
| Pore size, nm | 76 ± 15 |
| Average roughness, $R_a$, nm | 30 ± 6 |
| Thickness, nm | 647 ± 52 |
| Water contact angle natural light, degree | 60.6 ± 1.2 |
| Water contact angle with UV light, degree | 78.0 ± 6.0 |

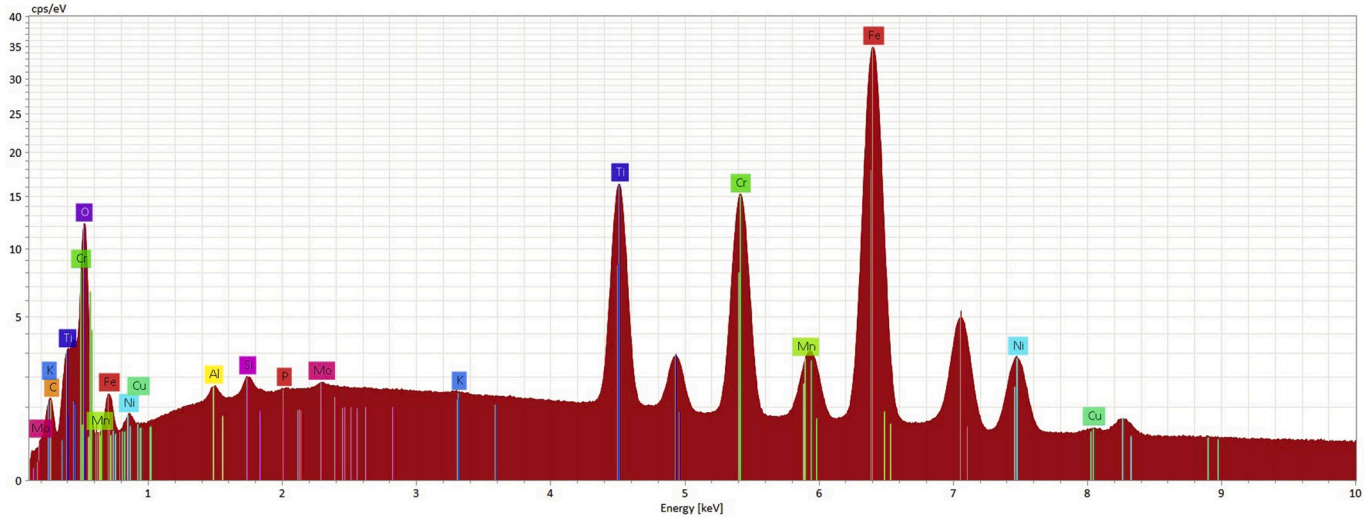


**Fig. 7.** Optimized coating's Energy-Dispersive X-ray Spectroscopy spectra. Observe the presence of the main components of the coating (titanium and oxygen) and the substrate (stainless steel).

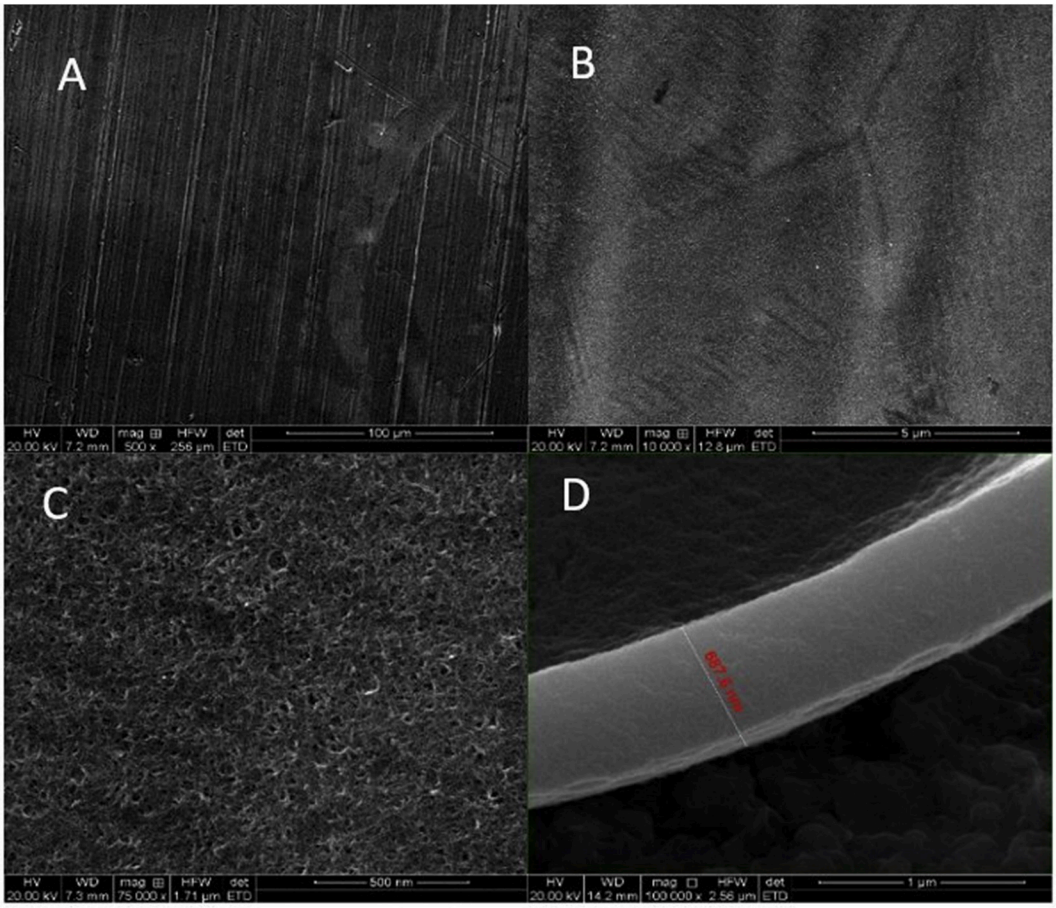


**Fig. 8.** Photocatalytically-optimized coating's topographic features. A) Macrostructure of the coating: observe how the AMC acquired the substrate's striations and defects. B) Microstructure of the coating: observe the three grain boundaries forming a vertex. C) Nanostructure of the coating: observe the pores formed after the sintering process. D) Coating thickness: ~690 nm.

finishing stainless steel. It can be observed that the coating adapted its shape to the striations, crevasses, and defects from the stainless steel substrate.

### 3.3.4. *Atomic force microscopy*

The photocatalytically-optimized coating exhibited irregular surface (30 nm average roughness, Ra) and conical pores. A typical pore, shown in Fig. 9, is approximately 100 nm diameter, resembling the pore size determined from SEM micrographs (76 ± 15 nm). There is general

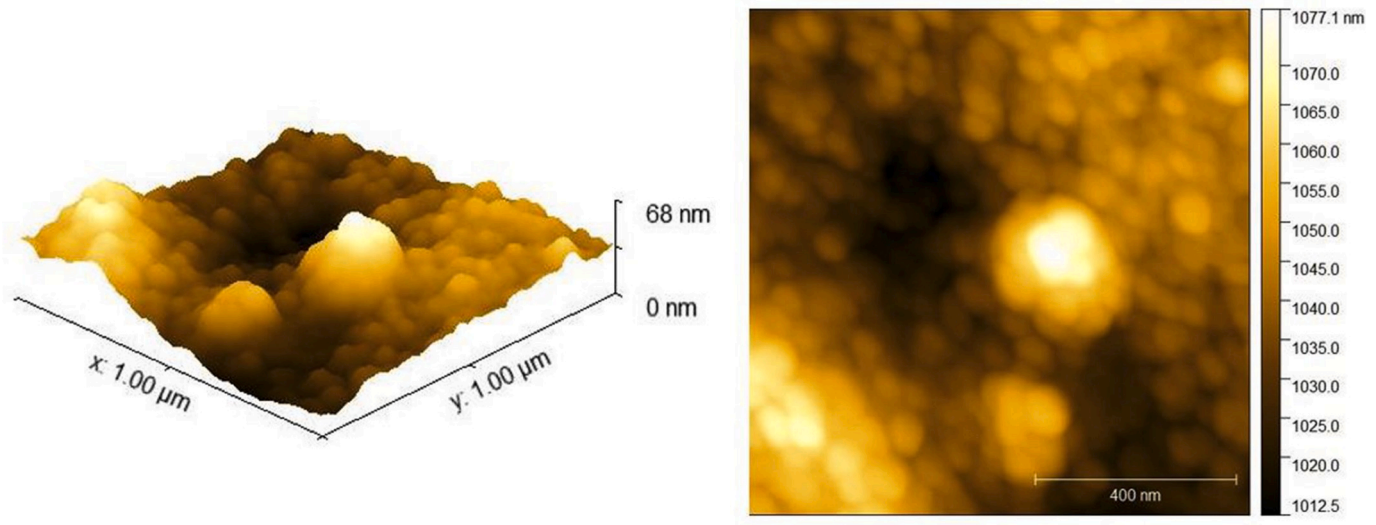


**Fig. 9.** Photocatalytically-optimized coating's surface profile by AFM. Observe that in addition to pores, the AMC also exhibits peaks of different heights.

agreement that surface roughness influences the ability of bacteria to adhere to surfaces. However, whether certain values of roughness and surface patterns promote or prevent bacterial adhesion is a matter of controversy. For example, Lüdecke and coworkers argue that on a nanometer scale, adhesion is reduced with increasing nanoroughness (~6 nm), but the opposite effect is observed with microroughness (>1 µm) [45]. On the other hand, Whitehead and coworkers indicate that attachment is microorganism-specific and not related to the surfaces' average roughness [46]. The roughness of the coating presented in this paper belongs to the nanoroughness scale, and therefore, may prevent bacterial adhesion.

#### 3.3.5. Composition determination

The complete removal of P123 from the matrix of the AMC after the sintering process at 507 °C was verified by EDS. Titanium and oxygen were the only two elements constituting the coating. Iron, chrome, magnesium, and traces of other metals were identified as well, but these elements corresponded to the stainless steel of the substrate.

### 3.4. Mechanical analysis

#### 3.4.1. Nanoindentation

The nanoindentation tests and wear assessment were performed on photocatalytic-optimized coatings deposited on stainless steel samples with mirror-like surface finish. The surface roughness of $TiO_2$ coatings deposited on stainless steel substrates with 2B finish created significant variability in the measured mechanical measurements because of the inconsistent contact area between the indenter tip and the rough substrate. The arithmetic average roughness, measured by optical profilometry, for mirror-like and 2B finishing substrates, was 14 nm and 181 nm, respectively. Mirror-like substrate finishes mitigated the effect of surface roughness on the measurement via nanoindentation of hardness, elastic modulus, and wear. The mechanical properties of the photocatalytic optimized coatings on stainless steel No. 8 mirror-like finishing were the following: hardness at 380 µN: 4.56 ± 0.19 GPa; Wear at 15 cycles: 400 nm; and Elastic modulus at 380 µN: 233 ± 10 GPa.

The hardness for the photocatalytically-optimized coating reported in this work is 4.6 GPa, harder than its stainless steel 304 substrate, which had an average hardness of 2.3 GPa. The photocatalytically-optimized coating's hardness is also similar to 1.0 GPa for a $TiO_2$ anatase coating by electrophoretic deposition reported by Hafedh [47], and 7.9 GPa for a nonporous $TiO_2$ anatase coating obtained by Comakli via sol-gel process using 500 °C of sintering temperature [21]. The difference between these values can be qualitatively explained considering that the strength of ceramic materials is correlated to the material's grain size in the following fashion [48]:

$$\sigma = kG^{-1/2} \tag{7}$$

where $\sigma$ is the strength (yield stress) (Pa), $k$ is the material specific Hall-Petch constant (Pa $m^{1/2}$), and G is the grain size (m). Equation (7) states that smaller grains give harder materials. For example, hardness decreased from 10 to 6 GPa [48] when grain size increased from 15 to 400 nm for single and polycrystalline $TiO_2$ rutile. Comakli and coworker's coating showed an average grain size of 42 nm while the coating presented here had grain sizes around 15 nm; hence, a harder coating was expected. However, the coating was determined to be softer, which is explained considering the other coating's parameters in addition to the grain size, such as the grain's shape, porosity, and crystal phase, which in turn, are englobed in the value of the Hall-Petch constant k in Equation (7).

The photocatalytically-optimized coating's elastic modulus is 233 GPa, higher than 190 GPa elastic modulus measured for the stainless steel 304 mirror-like substrate. The elastic modulus reported in this work is also higher than those reported for $TiO_2$ coatings by electrophoretic deposition with 108 GPa [47] and by sol-gel with 176 GPa of elastic modulus [31]. The elastic modulus $E$ was determined according to Equation (8):

$$E = \frac{\sqrt{\pi}}{2\sqrt{A(h)}}\left(\frac{dP}{dh}\right) \tag{8}$$

where $dP/dh$ represents the linear stiffness (N/m) during unloading, and $A(h)$ is the indenter's tip area as a function of penetration displacement, $h$. The elastic modulus was a function of coating depth, as can be observed in Fig. 10. For purpose of clarity, the elastic modulus values of one single test (out of 25) are shown. The measured elastic modulus continuously decreased with depth into the coating, as the strain field encountered the underlying stainless steel substrate [49]. Recall that the photocatalytically-optimized coating was around 650 nm thick. Therefore, elastic moduli captured from indentation of only less than 60 nm displacement were considered, which gave an average value of 233 GPa.

Hardness and elastic modulus values shown in are similar in magnitude to those assessed for similar anatase $TiO_2$ coatings [21,47,50], but well below rutile $TiO_2$ coatings whose values reach 12 GPa for hardness [51]. Higher hardness and elastic modulus may be seen as advantageous since these coatings may be more resilient, which could be

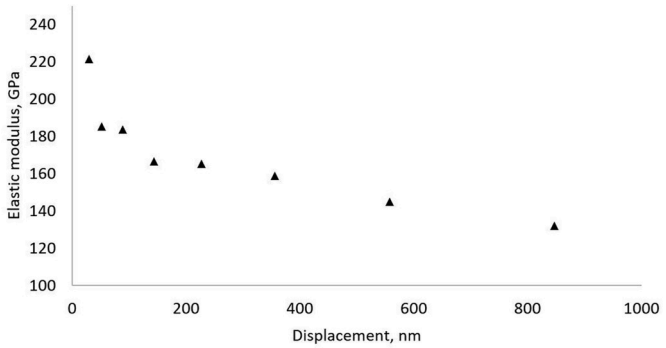


**Fig. 10.** The elastic modulus determined by nanoindentation decreased as the penetration depth increased, reaching values even lower than those of the stainless steel substrate. This figure shows elastic modulus values for a single test.

achieved by increasing the rutile phase in the coating. However, an increase in the rutile content of the $TiO_2$ coating would decrease the photocatalytic of the coating. Thus, an opportunity of optimization arises.

### 3.4.2. Wear assessment

Fig. 10 presents the wear resistance for two repetitions of the photocatalytically-optimized coating obtained via nanoindentation. A sapphire spherical tip was conducted via uniform wear cycles across the coating with a wear path of 100 μm, a constant load of 50 mN, and a velocity of 50 μm/s. These conditions allowed the indenter's tip to penetrate into the coating after the first cycle. When the first wear cycle was completed, an average plastic deformation of 10 nm was observed. The local minima in wear displacement of 402 nm was observed at the 15th cycle. The cyclic behavior of the wear displacement may be interpreted as an artifact originating from the accumulation of the coating material on the tip surface or within the wear path itself: after several wear cycles, the coating's material accumulated into the tip and then, some of this material was removed after subsequent cycles, starting the accumulation process again. This cyclic accumulation process could explain the positive (upwards) and the negative (downwards) displacements observed in Fig. 11 as well as the increasing size of the error bars.

Fig. 12 reveals some details to help understand what is occurring

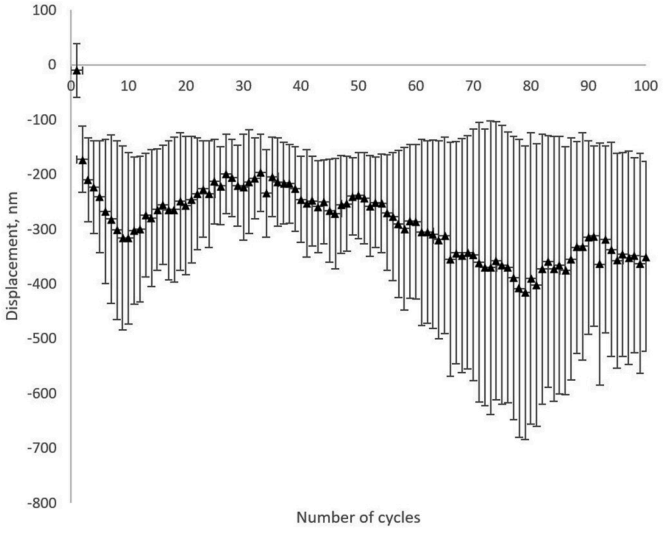


**Fig. 11.** Nano-wear experiment on photocatalytically-optimized photocatalyst. The cyclic behavior observed could be explained by $TiO_2$ accumulation on the tip used to perform the scratch across the photocatalyst's surface.

during the wear cycles. Along its path, the wear scratch crosses several substrate's striae. These striae come from the process from which the stainless steel was fabricated. As the nanoindenter's tip is dragged over the coating's surface, which has adapted its topography to the substrate, the wear of the coating followed by the wear of the underlying substrate at greater wear cycles are observed. If there is loose debris in the wear path, then that could account for the large error bars. The loose debris could reorient after each path, while producing a general trend of substrate wear underneath the debris. In addition to the striae of the substrate, the coating's irregularities also influence the erratic behavior of the indenter's tip. For example, it can be observed that the scratch lost its regular shape when cutting a fissure perpendicularly. The fissure caused the $TiO_2$ to enter the scratch. The presence of loose material and its subsequent accumulation at the interior of the scratch could be the reason of the continuous increase in size of the error bars depicted in Fig. 10.

For cleaning in place (CIP) systems, little mechanical stress is generated on the FCS since rinsing with hot water and detergents are the main features of such systems. Therefore, AMCs with low wear values are good enough. The same is not true for FCS sanitized via ice pigging or ice blasting, in which high shear stress is produced between the FCS and the blasting particles, and therefore, AMCs with low wear values are not convenient. The exact wear quantitative parameters needed for CIP systems and ice pigging are pending issues that need to be researched.

### 3.5. Comparison of the photocatalytic activity with values reported in the literature

A comparison between the obtained photocatalytic activity in the present study and values reported for photocatalytic activity of $TiO_2$ coatings tested under similar experimental conditions in the literature was performed. Sangpour and coworkers [52] explored the addition of noble metal nanoparticles to $TiO_2$ coatings deposited on quartz using magnetron sputtering. The photodecomposition of methylene blue was greatly increased from 0.072 ppm/h to 0.576 ppm for pure $TiO_2$ coatings and $TiO_2$ coatings with Ag and Cu nanoparticles, respectively. The doped effect was attributed to the increase in surface roughness and the presence of $Ti^{3+}$ oxygen vacancies formed due to the presence of the noble metal nanoparticles on the coating's surface. Lilja and partners [41] used vapor deposition to coat titanium with $TiO_2$. Degradation of the dye Rhodamine B was followed as a function of time. A pseudo first order degradation reaction was assumed, and the value of the constant rate $k = 5.63x10^{-4}$ $min^{-1}$ was considered as the descriptor of the photocatalytic activity. To make the comparison between photocatalytic activities straightforward, the values reported by Lilja were used to calculate the fading rate of $2.82x10^{-9}$ M/min for that coating. This photocatalytic activity was attributed by the authors to the roughness of the coating; we suggest that the result could also be due to the absence of pores. An additional paper reporting photocatalytic activity of $TiO_2$ in terms of methylene blue degradation was found, however, the reported values are expressed as decay rates [53], and did not allow direct comparison with our values.

### 3.6. Local optimum

Run 8 shown in Fig. 2 suggests that a photocatalytic activity local optimum may exist around the fabrication parameters combination of Protocol 2, Ti:EO 0.5 ratio, 1 h aging, 2000 rpm spinning speed, and 400 °C sintering temperature. To explore the possibility that the fabrication conditions of the optimal coating may enhance the value of the local optimum's photocatalytic activity, we fabricated additional coatings using the fabrication conditions for the photocatalytically-optimized coating, but with 1-h aging only (instead of nine, as used for the optimum). The fading speed obtained for these coatings was $3.79 \times 10^{-9} \pm 0.265$ M/min, which was lower than the fading speed that was attempted to be increased, namely, $4.48 \times 10^{-9} \pm 0.233$ M/min,

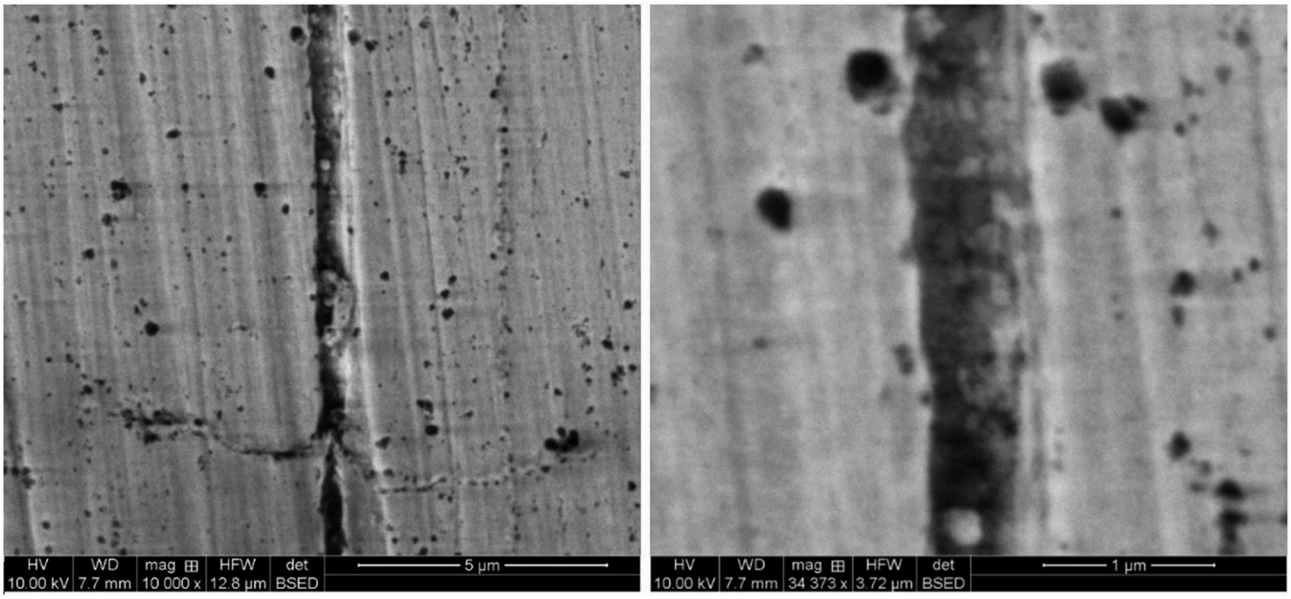


**Fig. 12.** SEM images showing details from the scratches performed via nanoindentation using a spherical diamond tip. Observe the irregularities along the scratch path and the accumulation of worn material at the interior of the scratch.

suggesting that the synthetic factors used to explore the local optimum were varied in the opposite direction required to increase the coating's photocatalytic activity.

## 4. Conclusions

The results presented in this work showed that the coating's microstructure and macrostructure influence, in a larger and lesser degree, respectively, the photocatalytic activity of the coating.

Among the microstructure describers, porosity plays a major role in the photocatalytic activity achieved. It was demonstrated that by varying the statistically significant synthetic parameters only, namely aging time and sintering temperature, it was possible to develop a coating whose photocatalytic activity presented a maximum within the experimental range explored in the present work. The combination that yielded this optimum (maximum) was 9 days of aging time and 507 °C.

The hardness and elastic modulus of the photocatalytically-optimized coating obtained in this work is higher than $TiO_2$ anatase-phase coatings deposited by electrophoretic deposition, but lower than nonporous $TiO_2$ anatase coatings. It should be realized that, although rutile $TiO_2$ coatings are by far more robust than anatase $TiO_2$ coatings, the former material has lower, if any, photocatalytic activity. Therefore, an optimal point of photocatalytic activity and robustness should be found with further research.

## Declaration of competing interest

The authors declare that they have no known competing financial interests or personal relationships that could have appeared to influence the work reported in this paper.

## CRediT authorship contribution statement

**Eduardo Torres Dominguez:** Writing - review & editing, Investigation, Methodology, Writing - original draft. **Phong Nguyen:** Writing - review & editing, Investigation, Methodology, Writing - original draft. **Annika Hylen:** Writing - review & editing, Investigation, Methodology, Writing - original draft. **Matthew R. Maschmann:** Writing - review & editing, Investigation, Methodology, Writing - original draft. **Azlin Mustapha:** Writing - review & editing, Investigation, Methodology, Writing - original draft. **Heather K. Hunt:** Writing - review & editing, Investigation, Methodology, Writing - original draft.

## Acknowledgments

E.T.D. gratefully acknowledges the U.S. Department of State through The Fulbright Program and the Comisión México-Estados Unidos para el Intercambio Educativo y Cultural (COMEXUS) for financial support through its graduate fellowship program.

## Appendix A. Supplementary data

Supplementary data to this article can be found online at https://doi.org/10.1016/j.matchemphys.2020.123001.

## References

[1] V.K. Yemmireddy, Y.-C. Hung, Using photocatalyst metal oxides as antimicrobial surface coatings to ensure food safety-opportunities and challenges, Compr. Rev. Food Sci. Food Saf. 16 (2017) 617–631.
[2] Y. Li, et al., Mechanism of photogenerated reactive oxygen species and correlation with the antibacterial properties of engineered metal-oxide nanoparticles, ACS Nano 6 (2012) 5164–5173.
[3] W. Eul, A. Moeller, N. Steiner, Hydrogen peroxide, in: Kirk-Othmer (Ed.), Kirk-Othmer Encyclopedia of Chemical Technology, John Wiley & Sons, 2001.
[4] J.M. Jay, M.J. Loessner, D.A. Golden, Modern food microbiology, in: Food Science Text Series, seventh ed., Springer, New York, 2005.
[5] N. Dhowlaghar, et al., Growth and biofilm formation by listeria monocytogenes in catfish mucus extract on four food contact surfaces at 22 and 10 degrees C and their reduction by commercial disinfectants, J. Food Protect. 81 (81) (2018) 59–67.
[6] V.K. Yemmireddy, Y.C. Hung, Using photocatalyst metal oxides as antimicrobial surface coatings to ensure food safety-opportunities and challenges, Compr. Rev. Food Sci. Food Saf. 16 (2017) 617–631.
[7] E.T. Dominguez, et al., Antimicrobial coatings for food contact surfaces: legal framework, mechanical properties, and potential applications, Compr. Rev. Food Sci. Food Saf. 18 (2019) 1825–1858.
[8] V.K. Yemmireddy, G.D. Farrell, Y.C. Hung, Development of titanium dioxide (TiO2) nanocoatings on food contact surfaces and method to evaluate their durability and photocatalytic bactericidal property, J. Food Sci. 80 (2015) 1903–1911.
[9] M. Bideau, et al., On the immobilization of titanium-dioxide in the photocatalytic oxidation of spent waters, J. Photochem. Photobil. 91 (1995) 137–144.
[10] US Congress, 21 CFR 110 - current good manufacturing practice in manufacturing, packaging for holding human food, in 21 CFR 2011, Fed. Regist. 66678-66680.
[11] European Parliament, Regulation (EC) No 1935/2004 of the European Parliament and of the Council of 27 October 2004 on Materials and articles intended to come into contact with food and repealing directives 80/590/EEC and 89/109/EEC, in

Regulation (EC) No 1935/2004, E. Parliament, Official Journal of the European Union (2004) L 338/4–L 338/17.
[12] Australia New Zealand Food Authority, A Guide to the Food Safety Standards, third ed., Food Standards Australia New Zealand, 2016.
[13] Secretaría de Salud, NORMA Oficial Mexicana NOM-251-SSA1-2009, Prácticas de higiene para el proceso de alimentos, bebidas o suplementos alimenticios, Diario Oficial de la Federación, 2010.
[14] F.R. Brotzen, Evaluation of mechanical properties of thin films, surface engineering, in: P.J. Blau (Ed.), ASM Handbook, ASM International, 1994, pp. 642–646.
[15] S.J. Bull, Microstructural characterization of coatings and thin films, surface engineering, in: P.J. Balu (Ed), ASM Handbook, ASM International, pp. 660–668.
[16] W.W.J. Zeno, N.J. Frank, Coatings, in: Kirk-Othmer (Ed.), Kirk-Othmer Encyclopedia of Chemical Technology, John Wiley & Sons, New York, 2013.
[17] R. Palanivelu, A.R. Kumar, Scratch and wear behaviour of plasma sprayed nano ceramics bilayer Al 2 O 3 -13 wt%TiO 2/hydroxyapatite coated on medical grade titanium substrates in SBF environment, Appl. Surf. Sci. 315 (315) (2014) 372–379.
[18] G. De Falco, et al., TIO2 nanoparticle coatings with advanced antibacterial and hydrophilic properties prepared by flame aerosol synthesis and thermophoretic deposition, Surf. Coating. Technol. 349 (2018) 830–837.
[19] M.A. Aegerter, Characterization of the mechanical properties of sol-gel coatings, in: L. Klein (Ed.), Handbook of Sol-Gel Science and Technology, Springer International Publishing, Saarbruecken, 2017.
[20] C.J. Brinker, G.W. Sherer, Sol-gel Science, the Physics and Chemistry of Sol-Gel Processing, Academic Press, New York, 1990, p. 912.
[21] O. Comakli, T. Yetim, A. Celik, The effect of calcination temperatures on wear properties of TiO2 coated CP-Ti, Surf. Coating. Technol. 246 (2014) 34–39.
[22] K.L. Avery, et al., Lysozyme sorption by pure-silica zeolite MFI films, Mater. Today Commun. 19 (19) (2019) 352–359.
[23] S. Mandal, A.D. Planells, H.K. Hunt, Impact of deposition and laser densification of Silicalite-1 films on their optical characteristics, Microporous Mesoporous Mater. 223 (223) (2016) 68–78.
[24] B.S. Goldschmidt, et al., Characterization of MgF2 thin films using optical tunneling photoacoustic spectroscopy, Optic Laser. Technol. 146 (73) (2015) 146–155.
[25] S. Atefyekta, et al., Antimicrobial performance of mesoporous titania thin films: role of pore size, hydrophobicity, and antibiotic release, Int. J. Nanomed. 11 (2016) 977–990.
[26] A.M. Collins, Nanotechnology Cookbook, Practical, Reliable and Jargon-free Experimental Procedures, first ed., Elsevier, Oxford, 2012, p. 312.
[27] V.N. Urade, et al., Controlling interfacial curvature in nanoporous silica films formed by evaporation-induced self-assembly from nonionic surfactants. II. Effect of processing parameters on film structure, Langmuir 23 (2007) 4268–4278.
[28] M.P. Tate, et al., How to dip-coat and spin-coat nanoporous double-gyroid silica films with EO19-PO43-EO19 surfactant (Pluronic P84) and know it using a powder X-ray diffractometer, Langmuir 26 (2010) 4357–4367.
[29] M. Yazici, et al., Effect of sol aging time on the wear properties of TiO2-SiO2 composite films prepared by a sol-gel method, Tribol. 104 (2016) 175–182.
[30] S. Sakka, Handbook of Sol-Gel Science and Technology, Processing, Characterization, and Applications, Kluwer Academic Publishers, Boston, 2004.
[31] O. Çomaklı, T. Yetim, A. Çelik, The effect of calcination temperatures on wear properties of TiO2 coated CP-Ti, Surf. Coating. Technol. 246 (2014) 34–39.
[32] Z.R. Lazic, Design of Experiments in Chemical Engineering, a Practical Guide, Wiley-VCH, Weinheim, 2004.
[33] P. Alexandridis, U. Olsson, B. Lindman, A record nine different phases (four cubic, two hexagonal, and one lamellar lyotropic liquid crystalline and two micellar solutions) in a ternary isothermal system of an amphiphilic block copolymer and selective solvents (water and oil), Langmuir 14 (1998) 2627–2638.
[34] S.S. Soni, et al., Quantitative SAXS analysis of the P123/water/ethanol ternary phase diagram, J. Phys. Chem. 110 (2006) 15157–15165.
[35] G. Wanka, H. Hoffmann, W. Ulbricht, Phase-Diagrams and aggregation behavior of poly(oxyethylene)-poly(oxypropylene)-poly(oxyethylene) triblock copolymers in aqueous-solutions, Macromolecules 27 (1994) 4145–4159.
[36] W.C. Oliver, G.M. Pharr, An improved technique for determining hardness and elastic-modulus using load and displacement sensing indentation experiments, J. Mater. Res. 7 (1992) 1564–1583.
[37] Standard Test Method for Film Hardness by Pencil Test, ASTM International, Pennsylvania, 2005.
[38] ISO 10678, Fine Ceramics (Advanced Ceramics, Advanced Technical Ceramics) — Determination of Photocatalytic Activity of Surfaces in an Aqueous Medium by Degradation of Methylene Blue, International Organization for Standardization, Geneva, 2010.
[39] ISO 10678, Fine Ceramics (Advanced Ceramics, Advanced Technical Ceramics) — Determination of Photocatalytic Activity of Surfaces in an Aqueous Medium by Degradation of Methylene Blue, International Organization for Standardization, Geneva, 2010.
[40] N. Le Bail, S. Benayoun, B. Toury, Mechanical properties of sol–gel coatings on polycarbonate: a review, J. Sol. Gel Sci. Technol. 75 (2015) 710–719.
[41] M. Lilja, et al., Photocatalytic and antimicrobial properties of surgical implant coatings of titanium dioxide deposited though cathodic arc evaporation, Biotechnol. Lett. 34 (2012) 2299–2305.
[42] D.S. Kim, S.-Y. Kwak, Photocatalytic inactivation of *E. coli* with a mesoporous TiO2 coated film using the film adhesion method, Environ. Sci. Technol. 43 (1) (2009) 148–151, 43.
[43] T. Theivasanthi, M. Alagar, Titanium dioxide (TiO2) nanoparticles - XRD analyses – an Insight, Centre Res. Post Graduate Dept. Phys. J. (2014). https://arxiv.org/pdf/1307.1091.pdf.
[44] Z. Zhang, Antimicrobial Coatings and Modifications on Medical Devices, Springer Science+Business Media, New York, 2017.
[45] C. Ludecke, et al., Nanorough titanium surfaces reduce adhesion of *Escherichia coli* and *Staphylococcus aureus* via nano adhesion points, Colloids Surf. B Biointerfaces 145 (2016) 617–625.
[46] K.A. Whitehead, et al., The effect of surface properties of polycrystalline, single phase metal coatings on bacterial retention, Int. J. Food Microbiol. 197 (2015) 92–97.
[47] D. Hafedh, K. Kaouther, B.C.L. Ahmed, Multi-property improvement of TiO2-WO3 mixed oxide films deposited on 316L stainless steel by electrophoretic method, Surf. Coating. Technol. 326 (2017) 45–52.
[48] R.W. Rice, Mechanical Properties of Ceramics and Composites, Grain and Particle Effects, Marcel Dekker, New York, 2000.
[49] A.C. Fischer-Cripps, Nanoindentation, third ed., Springer, New York, 2011.
[50] M. Kalisz, et al., Comparison of structural, mechanical and corrosion properties of TiO2-WO3 mixed oxide films deposited on TiAlV surface by electron beam evaporation, Appl. Surf. Sci. 421 (2017) 185–190.
[51] Y. Sun, Tribological rutile-TiO2 coating on aluminium alloy, Appl. Surf. Sci. 233 (2004) 328–335.
[52] P. Sangpour, F. Hashemi, A.Z. Moshfegh, Photoenhanced degradation of methylene blue on cosputtered M:TiO2 (M = Au, Ag, Cu) nanocomposite systems: a comparative study, J. Phys. Chem. C 114 (33) (2010) 13955–13961.
[53] P. Navabpour, et al., Photocatalytic TiO2 and doped TiO2 coatings to improve the hygiene of surfaces used in food and beverage processing—a study of the physical and chemical resistance of the coatings, Coatings 4 (2014) 433–449.